Preprints.org

Article

Not peer-reviewed version

Buckling Analysis of Variable-Angle Tow composite Plates Through Variable Kinematics Hierarchical Models

Gaetano Giunta * , Domenico Andrea Iannotta , Levent Kirkayak , Marco Montemurro

Posted Date: 16 May 2024

doi: 10.20944/preprints202405.1103.v1

Keywords: Buckling Analysis; Finite Element Method; Variable-Angle Tow Plates; Carrera's Unified Formulation; Reissner's Mixed Variational Theorem

Preprints.org is a free multidiscipline platform providing preprint service that is dedicated to making early versions of research outputs permanently available and citable. Preprints posted at Preprints.org appear in Web of Science, Crossref, Google Scholar, Scilit, Europe PMC.

Copyright: This is an open access article distributed under the Creative Commons Attribution License which permits unrestricted use, distribution, and reproduction in any medium, provided the original work is properly cited.

Preprints.org (www.preprints.org) | NOT PEER-REVIEWED | Posted: 16 May 2024 doi:10.20944/preprints202405.1103.v1

Disclaimer/Publisher's Note: The statements, opinions, and data contained in all publications are solely those of the individual author(s) and contributor(s) and not of MDPI and/or the editor(s). MDPI and/or the editor(s) disclaim responsibility for any injury to people or property resulting from any ideas, methods, instructions, or products referred to in the content.

Article

Buckling Analysis of Variable-Angle Tow Composite Plates through Variable Kinematics Hierarchical Models

Gaetano Giunta [1,*], Domenico Andrea Iannotta [1,2,3], Levent Kirkayak [1] and Marco Montemurro [3]

[1] Luxembourg Institute of Science and Technology, 5 avenue des Hauts-Fourneaux, L-4362 Esch-sur-Alzette, Luxembourg; domenico-andrea.iannotta@list.lu
[2] University of Luxembourg, Doctoral School in Science and Engineering (DSSE), 2 avenue de l'Université, L-4365 Esch-sur-Alzette, Luxembourg
[3] Arts et Métiers Institute of Technology, Université de Bordeaux, CNRS, INRA, Bordeaux INP, HESAM Université, I2M UMR 5295, F-33405 Talence, France; marco.montemurro@ensam.eu
* Correspondence: gaetano.giunta@list.lu

Abstract: Variable-Angle Tow (VAT) laminates can improve straight fiber composites mechanical properties thanks to the application of curvilinear fibers. This characteristic allows to achieve ambitious objectives for design and performance purposes. Nevertheless, the wider design space and the higher number of parameters result in a more complex structural problem. Among the various approaches that have been used for VATs study, Carrera's Unified Formulation (CUF) allows to obtain multiple theories within the same framework, guaranteeing a good compromise between the results accuracy and the computational cost. In this article, the linear buckling behavior of VAT laminates is analyzed through the extension of CUF 2D plate models within the Reissner's Mixed Variational Theorem (RMVT). Results show that RMVT can better approximate the prebuckling non-uniform stress field of the plate when compared to standard approaches, thus improving the prediction of the linear buckling loads of VAT composites.

Keywords: buckling analysis; finite element method; variable-angle tow plates; carrera's unified formulation; reissner's mixed variational theorem

1. Introduction

Composite materials have attracted considerable interest in various fields of application over the last decades. Thanks to their high stiffness-to-weight ratio, these materials gained great importance in those contexts where light structures with good mechanical properties are needed: this is the case of aerospace, automotive and construction industries. Despite this, a prevailing belief is that the optimal use of laminate structures can still be improved, in order to fully unlock the potential of fibres properties. For instance, when utilizing composites with straight fibers and a constant thickness, it becomes challenging to fully profit from the directional properties of this kind of materials. This limitation becomes especially problematic for complex geometries featuring geometrical discontinuities such as cut-outs. VAT plates are distinguished by the variation of fiber angles within the structure plane, which significantly enhances the design possibilities for a specific structure. Originally, VATs were produced using automated tape placement and automated fiber placement techniques [1]. Modern production techniques, such as Additive Manufacturing (AM) technologies, enable the overcoming of limitations related to automated processes, such as the existence of defects like overlaps. AM entails the incremental deposition of materials layer by layer to fabricate a three-dimensional object. In the context of VAT composites, AM processes are employed to deposit and cure layers of composite materials with varying fiber orientations, as explained by Zhuo et al. [2]. A key challenge in employing VATs lies in the complexity of the analysis. In such scenarios, it becomes essential to account for a higher number of variables, and during the optimization process, it is possible to end up with unfeasible fiber patterns.

© 2024 by the author(s). Distributed under a Creative Commons CC BY license.

Preprints.org (www.preprints.org) | NOT PEER-REVIEWED | Posted: 16 May 2024 doi:10.20944/preprints202405.1103.v1

The following is a concise summary of typical techniques employed in the analysis of the mechanical behavior of VATs, with particular emphasis on buckling investigations. One of the early methods made the assumption of constant fiber angle within each element in a Finite Element (FE) framework. This approach approximates the continuous variation of fiber direction discretely in a stepwise manner. Hyer and Lee in [3] used this technique to maximize the buckling load of a composite plate through a sensitivity analysis. The fibers angle corresponding to the maximum buckling load was identified for each element. Through a gradient-search technique, the influence of orientation changes on the buckling load was assessed. The buckling load was then optimized through recursive modifications of elements orientations, also considering the interactions between elements. However, a key limitation of these approaches arises from their reliance on an element-wise representation of the fiber paths. With this approach, the optimized solutions might exhibit fragmented fiber paths, making them impractical for manufacturing and necessitating a computationally expensive post-processing phase for adjustment [4]. A discrepancy between the structural responses computed based on the optimized fibers path and those computed after the optimized solution has undergone post-processing (recovery) has been often observed.

Gürdal et al. [5] utilized the classical lamination theory to analyze the mechanical response of VAT plates. They used the Rayleigh-Ritz method to conduct buckling analyses. The same method was applied by Oliveri and Milazzo [6] for analyzing the postbuckling behavior of VAT stiffened panels through the first-order shear deformation theory. The structures were modeled through the domain discretisation into plate-like subdomains by imposing boundary conditions for each component. Hao et al. [7] used the Mindlin plate theory within an isogeometric analysis to perform a linear buckling study of variable-stiffness panels, ensuring the continuity of fiber angle on the whole structure plane. Hao et al. [8] introduced a flow field function for the representation of fibers paths through a reduced numbers of variables. The buckling optimization of variable-stiffness composite panels with multiple cut-outs was performed through a bi-level optimization framework. In the first level, straight fiber paths with optimized orientation angles were first established to achieve a quasi-optimal design for maximizing buckling load and, in the second level, the flow field function was utilized to represent the fiber path. Raju et al. [9] used the Airy's stress function to accurately predict the prebuckling behavior of VAT plates. They used the differential quadrature method and the classical laminated plate theory to analyze the buckling response of VATs modelled. Sciascia et al. [10] studied VAT shells considering buckling, free vibrations and prestressed vibrations. The eigenvalue problem was solved through the Ritz formulation, while the shell kinematics was described with the first-order shear deformation theory. Chen et al. [11] presented an analytical model to predict the global, mixed and local buckling response of VAT plates with delaminations. The Rayleigh-Ritz approach was used to solve the prebuckling and buckling problems. Wu et al. [12] introduced a two-level optimization framework for the buckling of VAT plates. VATs were defined through lamination parameters represented by B-spline entities.

The Multi-Scale Two-Level (MS2L) approach leverages a dual-scale analysis of composite structures. It considers both micro and macro levels, enabling a detailed examination of material properties at the microscopic level while accounting for the overall structural behavior. This method allows to split the optimization problem into two levels. In the first step, the composite is considered as an equivalent homogeneous anisotropic plate, aiming to determine the optimal distribution of geometric and mechanical design variables governing VAT structure behavior at this scale. Among various macroscopic anisotropy representations, the most efficient one utilizes polar parameters (see Montemurro [13,14]). In the second step, the focus shifts to the mesoscopic scale and the objective is to identify at least one stack that aligns with the optimized arrangement of the polar parameters obtained from the initial optimization phase. The MS2L technique was applied by Montemurro and Catapano [15] with the aim of maximizing the buckling load of VAT plates. In the initial step, B-spline surfaces are used to represent the distribution of the polar parameters across the structure, while in the subsequent step, manufacturing constraints are taken into consideration. The initial framework

Preprints.org (www.preprints.org) | NOT PEER-REVIEWED | Posted: 16 May 2024 doi:10.20944/preprints202405.1103.v1

for the gradient-based optimization of VAT structures was introduced by Montemurro and Catapano in [16,17]. Its application to eigenvalue buckling problems was done by Fiordilino et al. [18], who introduced the analytical expression of the gradient of objective and constraint functions in buckling problems.

Carrera's Unified Formulation (CUF) has shown accurate results in the analysis of VATs. Considering plate geometries, CUF allows to choose a-priori the approximation functions along the thickness (Carrera [19,20]). Early works concerning CUF, presented the development of a Navier closed-form solution, which has been applied by Carrera et al. [21] and Carrera and Giunta [22] to perform, respectively, the static and failure analysis of isotropic plates under various loading conditions. Giunta et al. [23] used a Navier-type solution in order to perform the indentation failure analysis of composite sandwich plates. Giunta et al. [24] used CUF in order to study the linear buckling of thin-walled beams. Hui et al. [25] conducted a multiscale nonlinear analysis of composite beam structures using a series of one-dimensional (1D) CUF models. The asymptotic numerical method was employed to study the impact of microscopic imperfections on the macroscale response. Specifically, the influence of fiber defects was investigated by introducing sinusoidal geometries. By considering these imperfections, this work aimed to understand how they affect the overall behavior of the composite beam structures at a larger scale. A data-driven computational mechanics approach has been also employed with CUF models. In this context, Hui et al. [26] used 1D CUF models for static analysis of beam structures and found that the accuracy is dependent on the number of layers in the database. This demonstrates the potential for CUF models to be integrated with modern computing techniques. Viglietti et al. [27] and Fallahi et al. [28] employed a 1D CUF model to conduct free-vibration and buckling analyses of VAT structures, respectively. Fallahi et al. [29] further investigated buckling optimization in VATs using a genetic algorithm, applied to a one-dimensional CUF model. Sánchez-Majano et al. [30] studied the effects of manufacturing defects, such as varying fibre volume and fibre misalignments, on the buckling response of VAT plates. The Monte Carlo method was applied to perform stochastic buckling analyses. Pagani and Sánchez-Majano [31] incorporated Monte Carlo simulations and layer-wise CUF models in order to explore the impact of meso-scale fiber misalignments as defects in VAT laminates. The extension of CUF allows for the use of different expansions for each component of the displacement vector. This approach was demonstrated by Demasi et al. [32] for the study of VAT plates using triangular elements. Vescovini and Dozio [33] used Ritz's method within CUF for vibrational and buckling analyses of VATs. CUF offers an additional advantage through its compatibility with various variational formulations. Reissner's Mixed Variational Theorem, an alternative to the traditional Principle of Virtual Displacements, considers both displacements and out-of-plane transverse stresses as unknowns, demonstrating the flexibility of CUF in its applications. RMVT was widely used within CUF for the study of straight fibers composite structures. Carrera and Demasi [34] showed how to apply RMVT to CUF from a theoretical point of view, whereas in the second part of the article [35] static analyses were performed on straight fibers plates.

Inspired from the above works, the goal of this paper is to extend the previous works by Giunta et al. [36] and Iannotta et al. [37] on an RMVT-based family of plate finite elements within the CUF framework for dynamic and static analyses of VAT plates, respectively, to accurately predict buckling loads when curvilinear fibers are present.

The structure of the paper is as follows. Section 2 introduces the CUF approach and demonstrates its application to the two variational statements mentioned earlier. Section 3 considers three benchmark problems and performs linear buckling analyses with various loading conditions to discuss the differences between PVD and RMVT models and the reference solutions obtained in Abaqus using three-dimensional (3D) elements. Finally, Section 4 draws the conclusive remarks.

2. Carrera's Unified Formulation

A plate is a flat and thin structural element having in-plane dimensions significantly greater than its thickness. A global Cartesian reference system is considered to describe displacements, strains and

Preprints.org (www.preprints.org) | NOT PEER-REVIEWED | Posted: 16 May 2024 doi:10.20944/preprints202405.1103.v1

stresses. The x-axis and y-axis are aligned with the in-plane sides of the plate, whose dimensions are indicated as a and b, respectively. The z-axis is oriented perpendicular to the plane of the plate, in the same direction of the thickness h, which is negligible in comparison with a and b. The problem geometry and global reference system are illustrated in Figure 1.

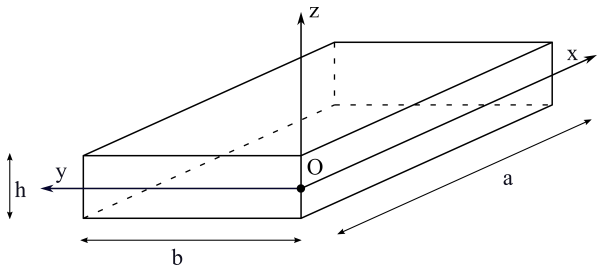

Figure 1. Plate geometry and reference system.

The displacement field is expressed as:

$$\mathbf{u} = \left\{ \begin{array}{c} u_x \\ u_y \\ u_z \end{array} \right\}. \tag{1}$$

The strain vector can be represented through Voigt's notation and, then, divided in its in-plane and out-of-plane components:

$$\boldsymbol{\epsilon}_p = \left\{ \begin{array}{c} \epsilon_{xx} \\ \epsilon_{yy} \\ \epsilon_{xy} \end{array} \right\}, \; \boldsymbol{\epsilon}_n = \left\{ \begin{array}{c} \gamma_{xz} \\ \gamma_{yz} \\ \gamma_{zz} \end{array} \right\}. \tag{2}$$

The assumption of small displacements permits the utilization of a linear relationship:

$$\begin{array}{l} \boldsymbol{\epsilon}_p = \mathbf{D}_p \mathbf{u} \, , \\ \boldsymbol{\epsilon}_n = (\mathbf{D}_{n\Omega} + \mathbf{D}_{nz}) \mathbf{u} \, , \end{array} \tag{3}$$

where $\mathbf{D}_p$, $\mathbf{D}_{n\Omega}$ and $\mathbf{D}_{nz}$ are the following differential operators:

$$\mathbf{D}_p = \left[\begin{array}{ccc} \frac{\partial}{\partial x} & 0 & 0 \\ 0 & \frac{\partial}{\partial y} & 0 \\ \frac{\partial}{\partial y} & \frac{\partial}{\partial x} & 0 \end{array} \right], \; \mathbf{D}_{n\Omega} = \left[\begin{array}{ccc} 0 & 0 & \frac{\partial}{\partial x} \\ 0 & 0 & \frac{\partial}{\partial y} \\ 0 & 0 & 0 \end{array} \right], \; \mathbf{D}_{nz} = \left[\begin{array}{ccc} \frac{\partial}{\partial z} & 0 & 0 \\ 0 & \frac{\partial}{\partial z} & 0 \\ 0 & 0 & \frac{\partial}{\partial z} \end{array} \right]. \tag{4}$$

The non-linear part of the strains can be introduced in a Green-Lagrange sense (see [38]):

$$\delta \epsilon_{ij}^{\mathrm{nl}} = \frac{1}{2} \left(\frac{\partial u_x}{\partial i} \frac{\partial u_x}{\partial j} + \frac{\partial u_y}{\partial i} \frac{\partial u_y}{\partial j} + \frac{\partial u_z}{\partial i} \frac{\partial u_z}{\partial j} \right) \text{ with } i, j = x, y, z. \tag{5}$$

The complete Cartesian components of strain can be obtained by summing the linear and non-linear terms. The in-plane and out-of-plane stress components can be written as:

$$\boldsymbol{\sigma}_p = \left\{ \begin{array}{c} \sigma_{xx} \\ \sigma_{yy} \\ \sigma_{xy} \end{array} \right\}, \; \boldsymbol{\sigma}_n = \left\{ \begin{array}{c} \sigma_{xz} \\ \sigma_{yz} \\ \sigma_{zz} \end{array} \right\}. \tag{6}$$

Preprints.org (www.preprints.org) | NOT PEER-REVIEWED | Posted: 16 May 2024 doi:10.20944/preprints202405.1103.v1

Hooke's law reads:

$$\begin{aligned} \boldsymbol{\sigma}_p &= \widetilde{\mathbf{C}}_{pp}\boldsymbol{\epsilon}_p + \widetilde{\mathbf{C}}_{pn}\boldsymbol{\epsilon}_n \,, \\ \boldsymbol{\sigma}_n &= \widetilde{\mathbf{C}}_{np}\boldsymbol{\epsilon}_p + \widetilde{\mathbf{C}}_{nn}\boldsymbol{\epsilon}_n \,, \end{aligned} \tag{7}$$

where the terms $\widetilde{\mathbf{C}}_{pp}$, $\widetilde{\mathbf{C}}_{pn}$, $\widetilde{\mathbf{C}}_{np}$ and $\widetilde{\mathbf{C}}_{nn}$ are the components of the material stiffness matrix.

2.1. Variable-Angle Tow Composite Plates

VAT laminates are characterized by a point-wise variation of the material stiffness matrix components along the in-plane directions. Because of the laminate stacking sequence, the material stiffness matrix is also subjected to a layer-wise variation along the thickness of the plate. The equation enabling the rotation of the material stiffness matrix $\mathbf{C}$ by a designated angle θ around the z-axis is expressed as follows:

$$\widetilde{\mathbf{C}} = \mathbf{T}\mathbf{C}\mathbf{T}^T \,. \tag{8}$$

Here, $\mathbf{C}$ denotes the material stiffness matrix in the material reference system, whereas $\widetilde{\mathbf{C}}$ represents the matrix after a rotation. The rotation matrix $\mathbf{T}$ is a function of the angle θ. For conciseness, the specific components of $\mathbf{C}$ and $\mathbf{T}$ are omitted in this context (refer to Reddy [38] for detailed information). A linear variation law can be formulated as:

$$\theta(\alpha) = \Phi + T_0 + \frac{T_1 - T_0}{d}|\alpha| \,. \tag{9}$$

The angle Φ represents the initial direction of variation for θ, α is a spatial variable given as:

$$\alpha = x' \cos(\Phi) + y' \sin(\Phi) \,. \tag{10}$$

where x' and y' denote the axes of the angle reference system. T_0 indicates the initial fiber angle when $\alpha = 0$, and T_1 represents the fiber angle when $\alpha = d$ as shown in Figure 2.

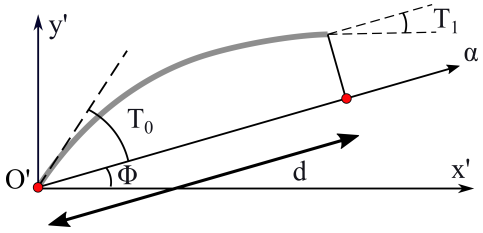

Figure 2. Example of in-plane fibers path.

Within this paper (and without loss of generality), the fibers angle is measured with respect to the x' axis. The direction of variation of θ can be along x', y' or a combination of theirs, depending on the specific case. The notation $\Phi < T_0, T_1 >$ is used to describe the in-plane path of the fibers, which is based on the parameters introduced earlier. More details about the variation law of the local fiber orientation can be found in Gürdal et al. [5].

2.2. Variational Formulation

The governing equations are here derived through the consideration of PVD and RMVT variational statements. The key distinction lies in PVD focusing solely on displacements as unknowns, whereas RMVT incorporates both displacements and transverse stresses, denoted as $\boldsymbol{\sigma}_n$, as primary unknowns. To effectively address the buckling problem, a prebuckling analysis is essential for determining the non-uniform stress distribution resulting from an external load. For the PVD case, the virtual internal work can be expressed as:

$$\delta L_i^{\text{PVD}} = \int_\Omega \int_h \left(\delta\boldsymbol{\epsilon}_{pG}^T \, \boldsymbol{\sigma}_{pH} + \delta\boldsymbol{\epsilon}_{nG}^T \, \boldsymbol{\sigma}_{nH} \right) dz \, d\Omega \,. \tag{11}$$

Preprints.org (www.preprints.org) | NOT PEER-REVIEWED | Posted: 16 May 2024 doi:10.20944/preprints202405.1103.v1

The subscript 'G' refers to components derived from geometrical relations outlined in Eqs. (3), whereas the subscript 'H' corresponds to components obtained through Hooke's law as specified in Eqs. (7). The term Ω represents the mid surface of the plate in the in-plane directions and the subscript 'T' stands for the transpose of a vector/matrix. The virtual internal work for the RMVT case is

$$\delta L_i^{\text{RMVT}} = \int_\Omega \int_h \left[\delta \boldsymbol{\epsilon}_{pG}^T \, \boldsymbol{\sigma}_{pH} + \delta \boldsymbol{\epsilon}_{nG}^T \, \boldsymbol{\sigma}_{nM} + \delta \boldsymbol{\sigma}_{nM}^T (\boldsymbol{\epsilon}_{nG} - \boldsymbol{\epsilon}_{nH}) \right] dz \, d\Omega \,, \tag{12}$$

where the 'M' subscript refers to the transverse stress components considered as primary unknowns in the mixed formulation. In the RMVT formulation, Hooke's law is expressed as follows:

$$\begin{aligned} \boldsymbol{\sigma}_{pH} &= \hat{\mathbf{C}}_{pp} \boldsymbol{\epsilon}_{pG} + \hat{\mathbf{C}}_{pn} \boldsymbol{\sigma}_{nM} \,, \\ \boldsymbol{\epsilon}_{nH} &= \hat{\mathbf{C}}_{np} \boldsymbol{\epsilon}_{pG} + \hat{\mathbf{C}}_{nn} \boldsymbol{\sigma}_{nM} \,, \end{aligned} \tag{13}$$

where $\hat{\mathbf{C}}_{pp}$, $\hat{\mathbf{C}}_{pn}$, $\hat{\mathbf{C}}_{np}$ and $\hat{\mathbf{C}}_{nn}$ are obtained by the following relations (see Carrera and Demasi [34]):

$$\begin{aligned} \hat{\mathbf{C}}_{pp} &= \widetilde{\mathbf{C}}_{pp} - \widetilde{\mathbf{C}}_{pn} \widetilde{\mathbf{C}}_{nn}^{-1} \widetilde{\mathbf{C}}_{np} \,, \\ \hat{\mathbf{C}}_{pn} &= \widetilde{\mathbf{C}}_{pn} \widetilde{\mathbf{C}}_{nn}^{-1} \,, \\ \hat{\mathbf{C}}_{np} &= -\widetilde{\mathbf{C}}_{nn}^{-1} \widetilde{\mathbf{C}}_{np} \,, \\ \hat{\mathbf{C}}_{nn} &= \widetilde{\mathbf{C}}_{nn}^{-1} \,. \end{aligned} \tag{14}$$

2.2.1. Prebuckling Problem

In the context of a prebuckling analysis, the following balance equation applies:

$$\delta L_i = \delta L_e \,, \tag{15}$$

where the virtual work associated with external loads reads:

$$\delta L_e = \int_{\Omega_p} \delta \mathbf{u}^T \, \mathbf{p} \, d\Omega \,, \tag{16}$$

where $\mathbf{p}$ is a surface load applied on the surface Ω_p at z coordinate z_p.

2.2.2. Linear Buckling Problem

The stress field obtained through the prebuckling analysis can be integrated for the computation of the pre-stresses virtual work δL_{σ^0} which reads:

$$\delta L_{\sigma^0} = \int_\Omega \int_h \left(\delta \epsilon_{xx}^{\text{nl}} \sigma_{xx}^0 + \delta \epsilon_{yy}^{\text{nl}} \sigma_{yy}^0 + \delta \epsilon_{xy}^{\text{nl}} \sigma_{xy}^0 + \delta \epsilon_{xz}^{\text{nl}} \sigma_{xz}^0 + \delta \epsilon_{yz}^{\text{nl}} \sigma_{yz}^0 + \delta \epsilon_{zz}^{\text{nl}} \sigma_{zz}^0 \right) dz \, d\Omega \,, \tag{17}$$

where σ_{ij}^0 are the pre-stresses energetically conjugate to the non-linear strains $\epsilon_{ij}^{\text{nl}}$, with $i, j = x, y, z$. The linear buckling problem can be written for both PVD and RMVT cases as:

$$\delta L_i = \delta L_{\sigma^0} \,. \tag{18}$$

2.3. Kinematic Assumption and Finite Element Approximation

CUF allows to introduce an axiomatic approximation in order to mathematically represent the primary unknowns along the direction parallel to the thickness (see Carrera [20]). Considering $f = f(x, y, z)$ as a generic unknown component, the following expansion can be introduced:

$$f(x, y, z) = F_\tau(z) g_\tau(x, y) \,, \quad \tau = 0, \, 1, \, \ldots, \, N \,. \tag{19}$$

In this context, f can represent solely a displacement component within a formulation derived by the PVD or a displacement or an out-of-plane stress component in the case of a RMVT formulation.

Preprints.org (www.preprints.org) | NOT PEER-REVIEWED | Posted: 16 May 2024 doi:10.20944/preprints202405.1103.v1

F_τ serves as an approximation function along the thickness, while g_τ represents an unknown two-dimensional function that approximates the in-plane variation. The used Einstein's notation assumes that a twice repeated index implies a sum over that index range. This notation simplifies mathematical expressions and calculations. N represents the approximation order, which can be chosen a-priori. Similarly, F_τ can also be imposed beforehand. The flexibility of the CUF enables the formulation of multiple theories within the same framework, making it a versatile tool for VATs analysis. Equivalent Single Layer (ESL) and Layer-Wise (LW) theories can be obtained through the adequate choice of F_τ and a coherent implementation of the layers stiffness matrices assembly.

2.3.1. Equivalent Single-Layer Theories

In the ESL framework, 1D polynomials of the type z^τ are used as F_τ in order to obtain Taylor's expansion for the representation of primary variables:

$$F_\tau(z) = z^\tau \ , \quad \tau = 0,\ 1,\ \ldots,\ N \ . \tag{20}$$

In this case, the number of layers does not affect the total number of unknowns. The components of the stiffness matrix are computed by summing the integrals of the thickness functions for each layer, each multiplied by its corresponding stiffness coefficient. Even if ESL models are characterized by a diminished computational complexity/cost and show a good prediction of thin laminates behavior, they lack in accuracy when thick plates are considered. Due to their reliance on C^∞ approximation functions, ESL approaches are unable to accurately capture the zigzag displacements effect. However, it might be feasible to incorporate this feature by introducing Murakami's function, as detailed in Carrera [39].

2.3.2. Layer-Wise Theories

Lagrange or Legendre polynomials can be used to approximate the unknown fields independently for each layer resulting, in this way, in a LW model for which it is possible to write the following approximation along the z-axis:

$$f^k(x,y,z) = F_b(z)g_b^k(x,y) + F_r(z)g_r^k(x,y) + F_t(z)g_t^k(x,y) \ , \quad r = 2,\ \ldots,\ N \ . \tag{21}$$

The superscript 'k' denotes a generic layer within the structure, with k ranging from one to N_l, where N_l represents the total number of layers. Subscripts 't' and 'b' correspond to the top and bottom faces of the generic layer, respectively. In the case of Legendre polynomials, the approximating functions along z-axis are:

$$F_t(z(\xi_k)) = \frac{P_0 + P_1}{2}, \quad F_b(z(\xi_k)) = \frac{P_0 - P_1}{2}, \quad F_r(z(\xi_k)) = P_r - P_{r-2}, \quad r = 2,\ \ldots,\ N \ , \tag{22}$$

where $P_i = P_i(\xi_k)$ represents the ith-order Legendre polynomial defined within the domain of the kth layer with the dimensionless through-the-thickness local coordinate ξ_k bounded within -1 and $+1$. LW models can accurately predict the zig-zag through-the-thickness behavior of the displacement field. However, they come with a higher computational cost, as the number of unknowns depends on the number of layers.

2.3.3. Finite Element Formulation

When a FE approximation is applied, it is necessary to incorporate the shape functions into the formulation. In the case of a 2D model, Eq (19) becomes:

$$f(x,y,z) = F_\tau(z)N_i(x,y)g_{\tau i} \ , \quad \tau = 0,\ 1,\ \ldots,\ N, \quad i = 1,\ \ldots,\ N_n \ , \tag{23}$$

Preprints.org (www.preprints.org) | NOT PEER-REVIEWED | Posted: 16 May 2024 doi:10.20944/preprints202405.1103.v1

where N_i denotes the shape functions of the element and N_n corresponds to the number of nodes utilized for the domain discretisation. Classical Lagrange shape functions are used. They are not explicitly detailed here for the sake of brevity and interested readers can refer to [40] for further information.

2.4. Acronym System

A comprehensive acronym system is implemented to identify the derived theories. The first letter designates the employed approximation level: 'E' corresponds to ESL models, while 'L' corresponds to LW models. The second letter denotes the variational statement: 'D' or 'M' signifies PVD or RMVT, respectively. The final number indicates the expansion order utilized along the plate thickness. If the first number is present, it signifies the number of virtual layers employed for the LW model to represent each physical layer. If the acronym begins without a numerical value, it is implicitly understood that only one virtual layer has been used for each physical layer. This system is shown in Figure 3.

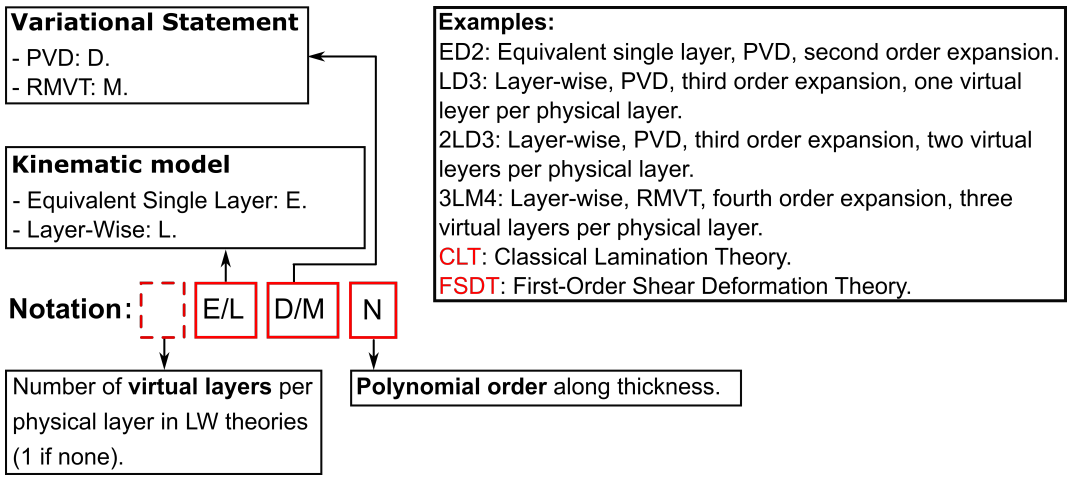

Figure 3. Acronym system.

For instance, the displacement field in EDN models corresponds to the following vectorial form:

$$\mathbf{u} = F_0\mathbf{u}_0 + F_1\mathbf{u}_1 + \cdots + F_N\mathbf{u}_N = F_\tau\mathbf{u}_\tau\,, \quad \tau = 0,\, 1,\, \ldots,\, N\,, \tag{24}$$

where $F_\tau = z^\tau$ and $\mathbf{u}_\tau = \mathbf{u}_\tau(x,y)$. Classical theories arise as specific cases of the ED1 solution: Classical Lamination Theory (CLT) and First-order Shear Deformation Theory (FSDT) are denoted as CLT and FSDT, respectively. FSDT is derived by penalizing the u_{z1} term in a first-order through-the-thickness approximation, whereas CLT requires penalization of the therms coming from the work of the transverse shear stresses. The material stiffness matrix is reduced to account for a plane stress state in both CLT and FSDT and avoid thickness locking.
For LDN solutions, only displacements are considered as unknowns:

$$\mathbf{u}^k = F_0\mathbf{u}_0^k + F_1\mathbf{u}_1^k + \cdots + F_N\mathbf{u}_N^k = F_\tau\mathbf{u}_\tau^k\,, \quad \tau = 0,\, 1\, \ldots,\, N\,, \quad k = 1,\, 2,\, \ldots,\, N_l\,. \tag{25}$$

For LMN solutions, also transverse stresses are included among the unknowns:

$$\boldsymbol{\sigma}_n^k = F_b\boldsymbol{\sigma}_b^k + F_r\boldsymbol{\sigma}_r^k + F_t\boldsymbol{\sigma}_t^k\,, \quad r = 2,\, \ldots,\, N\,, \quad k = 1,\, 2,\, \ldots,\, N_l\,. \tag{26}$$

In both cases, N refers to the approximation order employed in each layer. Noticeably, ESL theories can be viewed as specific instances of LW theories. In ESL, integration along the thickness is carried out to represent composite properties through an equivalent single layer. In contrast, in LW theories, integration is computed layer by layer. This allows for the individual representation of the

Preprints.org (www.preprints.org) | NOT PEER-REVIEWED | Posted: 16 May 2024 doi:10.20944/preprints202405.1103.v1

kinematics of each layer in LW models. Unless otherwise specified, LDN solutions are derived using Lagrange polynomials with equally spaced nodes, while LMN solutions utilize Legendre polynomials.

2.5. Stiffness Matrices Expression

Considering PVD, the displacement field groups the primary unknowns. In a PVD context, displacements from Eq (23) can be written as follows:

$$\mathbf{u} = F_\tau N_i \left\{ \begin{array}{c} q_{x\tau i} \\ q_{y\tau i} \\ q_{z\tau i} \end{array} \right\} = F_\tau N_i \mathbf{q}_{\tau i} \ . \tag{27}$$

Through the substitution of Eqs. (3), (7), (27) and (11) into Eqs. (18), the PVD governing equations are obtained:

$$\begin{aligned} &\int_\Omega \delta \boldsymbol{q}_{\tau i}^T \big(\mathbf{D}_p^T(N_i\mathbf{I}) \widetilde{\mathbf{Z}}_{pp}^{\tau s} \mathbf{D}_p(N_j\mathbf{I}) + \mathbf{D}_p^T(N_i\mathbf{I}) \widetilde{\mathbf{Z}}_{pn}^{\tau s} \mathbf{D}_{n\Omega}(N_j\mathbf{I}) + \mathbf{D}_p^T(N_i\mathbf{I}) \widetilde{\mathbf{Z}}_{pn}^{\tau s_{,z}}(N_j\mathbf{I}) + \\ &+ \mathbf{D}_{n\Omega}^T(N_i\mathbf{I}) \widetilde{\mathbf{Z}}_{np}^{\tau s} \mathbf{D}_p(N_j\mathbf{I}) + \mathbf{D}_{n\Omega}^T(N_i\mathbf{I}) \widetilde{\mathbf{Z}}_{nn}^{\tau s} \mathbf{D}_{n\Omega}(N_j\mathbf{I}) + \mathbf{D}_{n\Omega}^T(N_i\mathbf{I}) \widetilde{\mathbf{Z}}_{nn}^{\tau s_{,z}}(N_j\mathbf{I}) + \\ &+ (N_i\mathbf{I}) \widetilde{\mathbf{Z}}_{np}^{\tau_{,z} s} \mathbf{D}_p(N_j\mathbf{I}) + (N_i\mathbf{I}) \widetilde{\mathbf{Z}}_{nn}^{\tau_{,z} s} \mathbf{D}_{n\Omega}(N_j\mathbf{I}) + (N_i\mathbf{I}) \widetilde{\mathbf{Z}}_{nn}^{\tau_{,z} s_{,z}}(N_j\mathbf{I}) \big) \boldsymbol{q}_{sj} d\Omega = \delta L_{\sigma^0} \ , \end{aligned} \tag{28}$$

where:

$$\left(\widetilde{\mathbf{Z}}_{wr}^{\tau s}, \widetilde{\mathbf{Z}}_{wr}^{\tau_{,z} s}, \widetilde{\mathbf{Z}}_{wr}^{\tau s_{,z}}, \widetilde{\mathbf{Z}}_{wr}^{\tau_{,z} s_{,z}} \right) = \left(\widetilde{\mathbf{C}}_{wr} E_{\tau s}, \widetilde{\mathbf{C}}_{wr} E_{\tau_{,z} s}, \widetilde{\mathbf{C}}_{wr} E_{\tau s_{,z}}, \widetilde{\mathbf{C}}_{wr} E_{\tau_{,z} s_{,z}} \right) : \ w,r = p,n \ , \tag{29}$$

$$(E_{\tau s}, E_{\tau_{,z} s}, E_{\tau s_{,z}}, E_{\tau_{,z} s_{,z}}) = \int_h (F_\tau F_s, F_{\tau_{,z}} F_s, F_\tau F_{s_{,z}}, F_{\tau_{,z}} F_{s_{,z}}) dz \ . \tag{30}$$

Index 'z' when preceded by a comma refers to the derivative along z-axis. In a compact vectorial form, Eq (28) reads:

$$\delta \boldsymbol{q}_{\tau i}^T \mathbf{K}^{\tau s ij} \boldsymbol{q}_{sj} = \delta L_{\sigma^0} \ , \tag{31}$$

where $\mathbf{K}^{\tau s ij}$ is a 3×3 Fundamental Nucleus (FN). The loops on the indices τ, s, i and j allow to build the stiffness matrix of the whole plate element expanding over the kinematic approximation and the finite element approximation, respectively.
In the RMVT case, also transverse stresses constitute an unknown field:

$$\boldsymbol{\sigma}_n = F_\tau N_i \left\{ \begin{array}{c} g_{xz\tau i} \\ g_{yz\tau i} \\ g_{zz\tau i} \end{array} \right\} = F_\tau N_i \mathbf{g}_{\tau i} \ . \tag{32}$$

Through the substitution of Eqs. (3), (13), (27), (32) and (12) into Eqs. (18), the governing equations of the RMVT can be written as follows:

$$\begin{aligned} &\int_\Omega \delta \boldsymbol{q}_{\tau i}^T \big[\mathbf{D}_p^T(N_i\mathbf{I}) \hat{\mathbf{Z}}_{pp}^{\tau s} \mathbf{D}_p(N_j\mathbf{I}) \big] \boldsymbol{q}_{sj} + \delta \boldsymbol{q}_{\tau i}^T \big[\mathbf{D}_p^T(N_i\mathbf{I}) \hat{\mathbf{Z}}_{pn}^{\tau s}(N_j\mathbf{I}) + \mathbf{D}_{n\Omega}^T(N_i\mathbf{I}) (E_{\tau s}\mathbf{I}) (N_j\mathbf{I}) + \\ &+ (N_i\mathbf{I}) (E_{\tau_{,z} s}\mathbf{I}) (N_j\mathbf{I}) \big] \boldsymbol{g}_{sj} + \delta \boldsymbol{g}_{\tau i}^T \big[(N_i\mathbf{I}) (E_{\tau s}\mathbf{I}) \mathbf{D}_{n\Omega}(N_j\mathbf{I}) + (N_i\mathbf{I}) (E_{\tau s_{,z}}\mathbf{I}) (N_j\mathbf{I}) + \\ &- (N_i\mathbf{I}) \hat{\mathbf{Z}}_{np}^{\tau s} \mathbf{D}_p(N_j\mathbf{I}) \big] \boldsymbol{q}_{sj} - \delta \boldsymbol{g}_{\tau i}^T (N_i\mathbf{I}) \hat{\mathbf{Z}}_{nn}^{\tau s}(N_j\mathbf{I}) \boldsymbol{g}_{sj} d\Omega = \delta L_{\sigma^0} \ , \end{aligned} \tag{33}$$

where:

$$(\hat{\mathbf{Z}}_{wr}^{\tau s}, \hat{\mathbf{Z}}_{wr}^{\tau_{,z} s}, \hat{\mathbf{Z}}_{wr}^{\tau s_{,z}}, \hat{\mathbf{Z}}_{wr}^{\tau_{,z} s_{,z}}) = (\hat{\mathbf{C}}_{wr} E_{\tau s}, \hat{\mathbf{C}}_{wr} E_{\tau_{,z} s}, \hat{\mathbf{C}}_{wr} E_{\tau s_{,z}}, \hat{\mathbf{C}}_{wr} E_{\tau_{,z} s_{,z}}) : \ w,r = p,n \ . \tag{34}$$

Preprints.org (www.preprints.org) | NOT PEER-REVIEWED | Posted: 16 May 2024 doi:10.20944/preprints202405.1103.v1

In a compact form:

$$\begin{aligned}\delta \boldsymbol{q}_{\tau i}^{T} \mathbf{K}_{uu}^{\tau sij} \boldsymbol{q}_{sj} + \delta \boldsymbol{q}_{\tau i}^{T} \mathbf{K}_{u\sigma}^{\tau sij} \boldsymbol{g}_{sj} = \delta L_{\sigma^0} \ , \\ \delta \boldsymbol{g}_{\tau i}^{T} \mathbf{K}_{\sigma u}^{\tau sij} \boldsymbol{q}_{sj} + \delta \boldsymbol{g}_{\tau i}^{T} \mathbf{K}_{\sigma\sigma}^{\tau sij} \boldsymbol{g}_{sj} = 0 \ .\end{aligned} \tag{35}$$

In this case, four fundamental nuclei are obtained. Gauss quadrature has been used to compute the in-plane integrals. Due to the varying stiffness coefficients of the materials, the number of Gauss points must be adjusted for a given analytical formula describing the local fibers orientation to ensure converged integration. A reduced integration is used to correct the shear locking phenomenon. A 4×4 grid of Gauss points is used for the fully integrated terms, while a 2×2 grid is used for the reduced ones. Through the substitution of Eqs. (5) and (27) into Eqs. (17), it is possible to obtain the pre-stresses virtual work:

$$\begin{aligned}\delta L_{\sigma^0} = \int_{\Omega} \int_{h} \boldsymbol{q}_{\tau i}^{T} \big[F_{\tau} F_{s} N_{i,x} N_{j,x} \sigma_{xx}^{0} + F_{\tau} F_{s} N_{i,y} N_{j,y} \sigma_{yy}^{0} + F_{\tau} F_{s} \Big(N_{i,x} N_{j,y} + N_{i,y} N_{j,x} \Big) \sigma_{xy}^{0} + \\ + \big(F_{\tau} F_{s_{,z}} N_{i,x} N_{j} + F_{\tau_{,z}} F_{s} N_{i} N_{j,x} \big) \sigma_{xz}^{0} + \Big(F_{\tau} F_{s_{,z}} N_{i,y} N_{j} + F_{\tau_{,z}} F_{s} N_{i} N_{j,y} \Big) \sigma_{yz}^{0} + \\ + F_{\tau_{,z}} F_{s_{,z}} N_{i} N_{j} \sigma_{zz}^{0} \big] \mathbf{I} \boldsymbol{q}_{sj} dz d\Omega \ .\end{aligned} \tag{36}$$

In a compact form it reads:

$$\delta L_{\sigma^0} = \delta \boldsymbol{q}_{\tau i}^{T} \mathbf{K}_{\sigma^0}^{\tau sij} \boldsymbol{q}_{sj} \ , \tag{37}$$

where $\mathbf{K}_{\sigma^0}^{\tau sij}$ is the fundamental nuclues of the geometric stiffness matrix.

3. Numerical Results

This section presents some numerical investigations to assess the proposed finite element formulation. Three benchmark cases are considered: a monolayer plate, a multilayer plate and a multilayer plate with a central circular cut out. For all the cases, a square plate ($a = b$) is considered, whereas different boundary and load conditions are applied in order to obtain a variety of results as wide as possible. Two materials are used whose properties are represented in Table 1.

Table 1. Material properties.

Case	E_L [GPa]	E_T [GPa]	G_{LT} [GPa]	G_{TT} [GPa]	ν_{LT}, ν_{TT}
1	50	10	5	5	0.25
2, 3	181	10.27	7.17	3.78	0.28

Where 'L' and 'T' stand for longitudinal and transverse direction, respectively. Abaqus 3D models are deve as reference solutions. For these models, the mesh is constituted by quadratic solid elements with reduced integration and three degrees of freedom per node (C3D20R). A refined in-plane mesh is needed to obtain accurate results in Abaqus due to the element-wise constant orientation of the fibres. Nine-node square elements (QUAD9) are used for CUF solutions. Results are presented in terms of an equivalent critical force F_i^{cr} for the ith buckling mode defined as:

$$F_i^{cr} = \lambda_i a h \ , \tag{38}$$

where λ_i is the ith buckling eigenvalue represenative of an applised lateral surface load (whose units are [Pa]).

The following equation is used to compute the percentage errors:

Preprints.org (www.preprints.org) | NOT PEER-REVIEWED | Posted: 16 May 2024 doi:10.20944/preprints202405.1103.v1

$$\delta_i = \frac{|F^{cr}_{i,\text{CUF}} - F^{cr}_{i,\text{Abaqus3D}}|}{|F^{cr}_{i,\text{Abaqus3D}}|} \cdot 100 \,. \tag{39}$$

3.1. Monolayer Plate

The first benchmark problem is a monolayer plate characterized by the following dimensions: $a = b = 1$ m, $h = 0.01$ m. Fibers angle is represented as a function of y'. In this case, the local frame of the fibers path is aligned with the global reference frame of the structure. Hence, the characteristic length in Eq. (9) is set as $d = b$. Figure 4 represents the law of fibres angle, which can be written as $90 < 0, 90 >$. This law is taken from Viglietti et al. [27], where it is applied on a rectangular plate for vibration analyses.

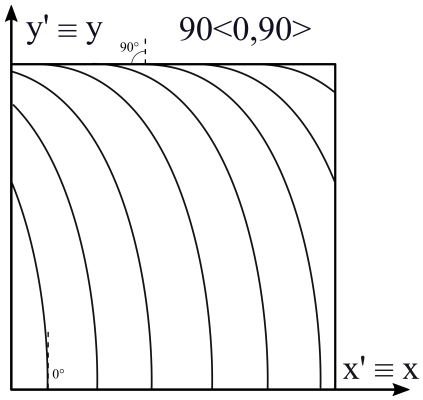

Figure 4. In-plane fibers variation path, case 1.

The plate is clamped in correspondence of the side where $y/b = 0$, while only the displacement u_y is free at $y = b$. A constant pressure $P^0_{yy} = 1$ Pa is applied at $y = b$, as shown in Figure 5.

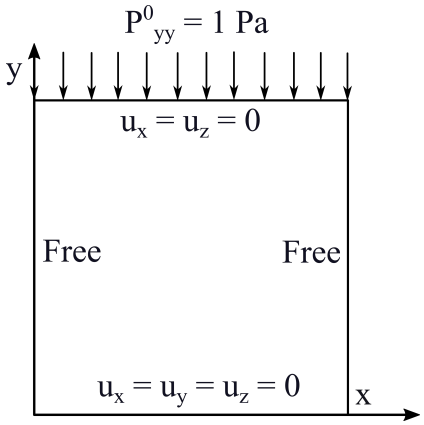

Figure 5. Boundary and loading conditions, case 1.

Abaqus reference solution contains 80 elements along each side and 16 elements along the thickness. Table 2 shows the results of the preliminary convergence analysis, considering the ED2 model. The first four buckling loads are shown for each mesh, together with the number of Degrees Of Freedom (DOF). It is possible to observe that by increasing the number of in-plane elements, the results get progressively closer to the reference solution. The 8×8 mesh is considered as the best compromise between computational cost and results accuracy, for this reason it is used in the following analyses in order to study the behavior of higher-order CUF theories.

Preprints.org (www.preprints.org) | NOT PEER-REVIEWED | Posted: 16 May 2024 doi:10.20944/preprints202405.1103.v1

Table 2. Comparison of DOF and critical loads F_i^{cr} [N] between Abaqus 3D and ED2 mesh, case 1.

	DOF	$F_1^{cr} \cdot 10^{-3}$	$F_2^{cr} \cdot 10^{-3}$	$F_3^{cr} \cdot 10^{-3}$	$F_4^{cr} \cdot 10^{-3}$
Abaqus 3D	1,310,499	28.926	57.366	85.585	122.498
2×2	225	29.901	57.475	136.926	170.607
4×4	729	28.126	55.545	88.768	125.994
6×6	1521	28.333	56.023	85.550	122.138
8×8	2601	28.473	56.323	85.196	121.744
10×10	3969	28.565	56.524	85.160	121.739

Table 3 shows the DOF for different theories and expansion orders. FSDT and CLT show the smallest number of DOF. Because of the way in which they are modeled through CUF, FSDT and CLT theories have the same number of DOF. It is possible to observe that mixed CUF models, which can be considered as the computationally most expensive ones, are characterized by a number of DOF which is two magnitude orders smaller than the Abaqus reference solution.

Table 3. Number of degrees of freedom, case 1.

Model	**DOF**
Abaqus 3D	1,310,499
3LM4	22,542
3LM2	12,138
3LD4	11,271
3LD2	6069
ED4	4335
ED2	2601
FSDT	1734
CLT	1734

In order to retrieve the plate non-uniform stress field when a compression load is applied, a prebuckling analysis is performed. Figures 6, 7 and 8 show the in-plane contour plots of the in-plane displacement u_y^0 and the in-plane normal stresses σ_{xx}^0 and σ_{yy}^0, respectively. The comparison between 3LM4 and Abaqus 3D results can be observed, showing a good agreement between the two approaches.

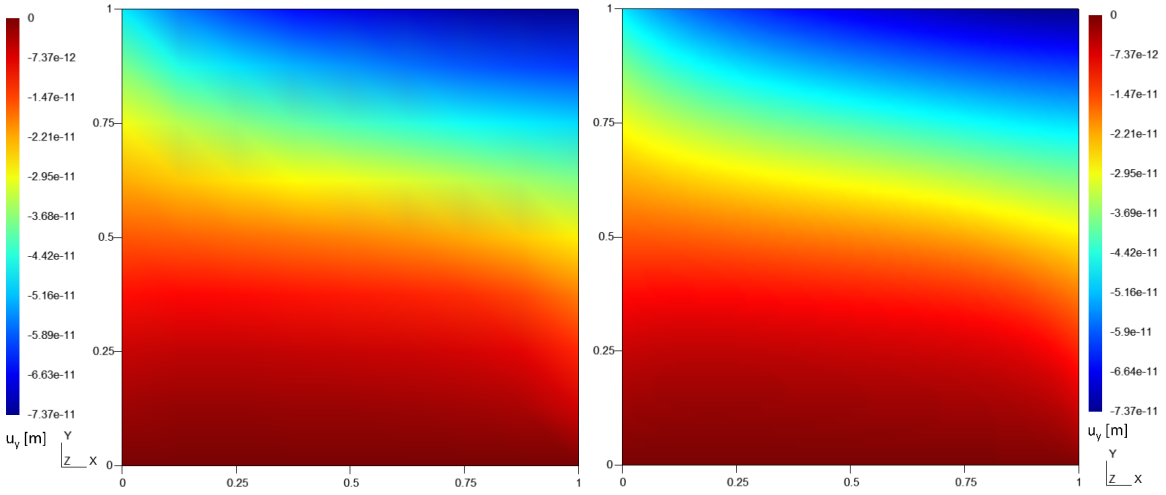

(**a**) 3LM4 (**b**) Abaqus 3D

Figure 6. Contour plots of the displacement along y axis u_y^0 [m], case 1.

Preprints.org (www.preprints.org) | NOT PEER-REVIEWED | Posted: 16 May 2024 doi:10.20944/preprints202405.1103.v1

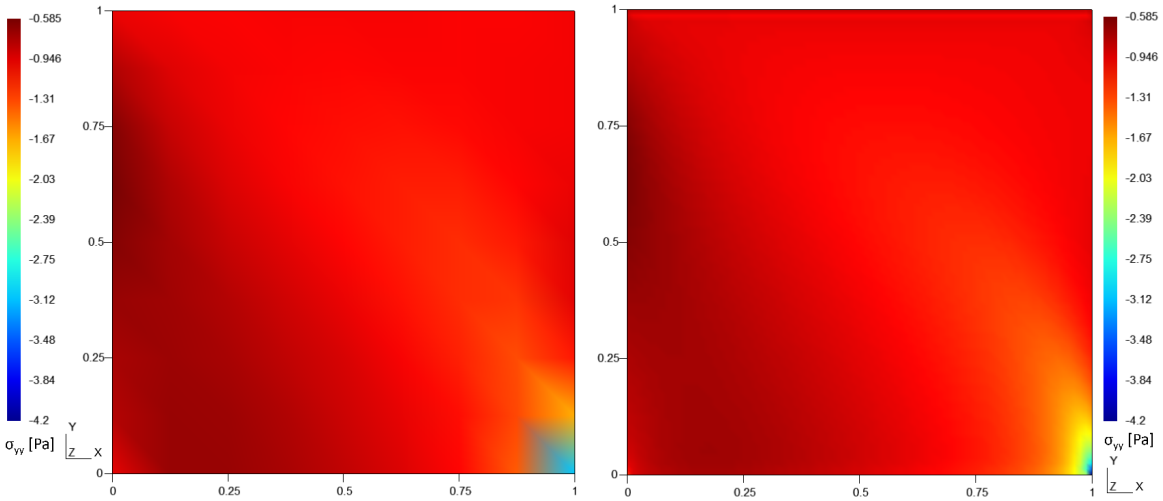

(**a**) 3LM4 (**b**) Abaqus 3D

Figure 7. Contour plots of the in-plane normal stress σ^0_{yy} [Pa], case 1.

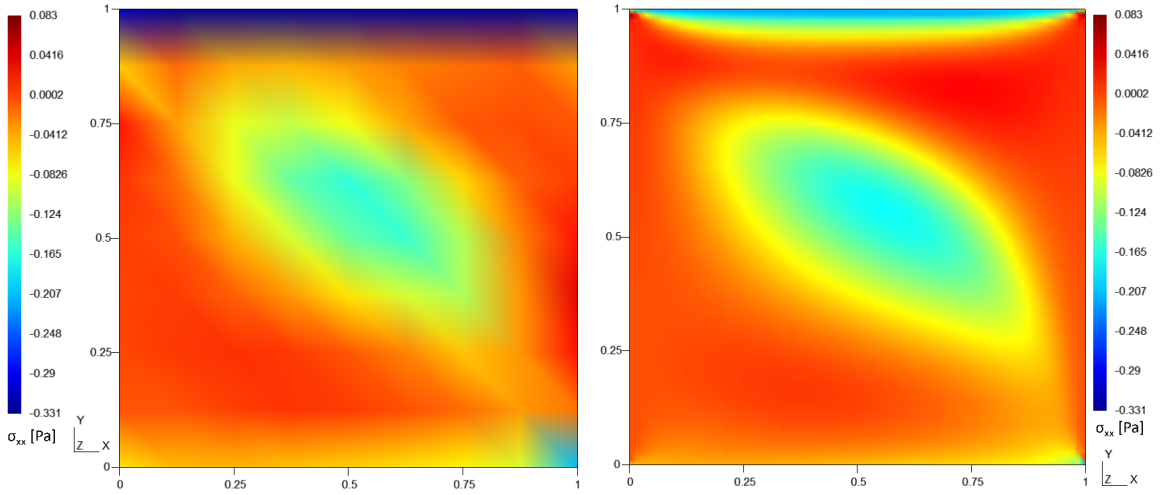

(**a**) 3LM4 (**b**) Abaqus 3D

Figure 8. Contour plots of the in-plane normal stress σ^0_{xx} [Pa], case 1.

Table 4 shows the first four critical loads for different theories. The CLT model is not able to predict the buckling loads of the plate and it is not reported in the table. This behavior allows to observe the importance of transverse shear stresses for this case, which can not be computed through CLT. The approximation given by the FSDT model shows a percentage error of 5.3% on the first buckling load. This error can be reduced to 1.6% through an ED2 model. 3LD2 and 3LD4 models show a similar approximation, since they both show an error of 0.2% on the first buckling load. The best approximation of the first critical load is given by 3LM2 and 3LM4 models, which show an error of 0.1%. As far as the higher critical loads are concerned, LM models are closer to the reference solution.

Preprints.org (www.preprints.org) | NOT PEER-REVIEWED | Posted: 16 May 2024 doi:10.20944/preprints202405.1103.v1

Table 4. Critical loads F_i^{cr} [N], case 1.

	$F_1^{cr} \cdot 10^{-3}$	$F_2^{cr} \cdot 10^{-3}$	$F_3^{cr} \cdot 10^{-3}$	$F_4^{cr} \cdot 10^{-3}$
Abaqus 3D	28.926	57.366	85.585	122.498
3LM4	28.962	57.319	85.796	122.756
3LM2	28.958	57.309	85.788	122.743
3LD4	28.979	57.478	85.891	122.928
3LD2	28.979	57.479	85.892	122.929
ED4	28.468	56.296	85.154	121.683
ED2	28.473	56.323	85.196	121.744
FSDT	30.461	59.571	90.594	128.661

3.2. Multilayer Plate

The second benchmark problem is a multilayer plate is considered and it has been taken from Hao et al. [7]. It has been also studied by Fallahi et al. [28]. The plate is square and composed of sixteen layers with of equal thickness. In-plane dimension are $a = b = 254$ mm and each ply has a thickness of 0.15 mm. Fibers angle is expressed as a function of the x'-axis. Axes x' and y' of the local reference system of the fibers path are parallel to axes x and y of the global reference system of the plate, but they are translated such that their origin is located at the center of the plate $(a/2, b/2)$. In this case, the characteristic length in Eq. (9) is $a/2$, hence $d = a/2$. A symmetric and balanced stack is considered with the following fibers path parameters: $[0 < 60, 15 > |0 < -60, -15 > |0 < -60, -15 > |0 < 60, 15 >]_4$. The stacking sequence is represented in Figure 9 for the representative layers $0 < 60, 15 >$ and $0 < 60, -15 >$ in the symmetric pattern.

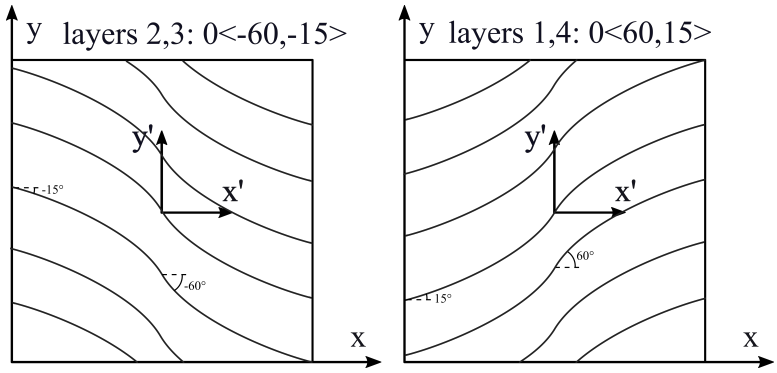

Figure 9. In-plane fibers path and stacking sequence, case 2.

As for the previous case, the Abaqus reference solution contains 80 elements along each side and 16 elements along the thickness. For CUF results, a 8×8 mesh is considered. At each side of the plate, the displacement along z axis is equal to zero ($u_z = 0$). At the lower left corner $(0, 0)$ also the displacement along y is zero ($u_y = 0$), while at the lower right corner $(a, 0)$ all the displacements are constrained ($u_x = u_y = 0$). Two loading conditions are considered: a pure compression case along x axis ($P_{xx}^0 = 1$ Pa) and a combined compression-shear case ($P_{xx}^0 = P_{xy}^0 = 1$ Pa). Boundary and loading conditions are shown in Figure (10).

Preprints.org (www.preprints.org) | NOT PEER-REVIEWED | Posted: 16 May 2024 doi:10.20944/preprints202405.1103.v1

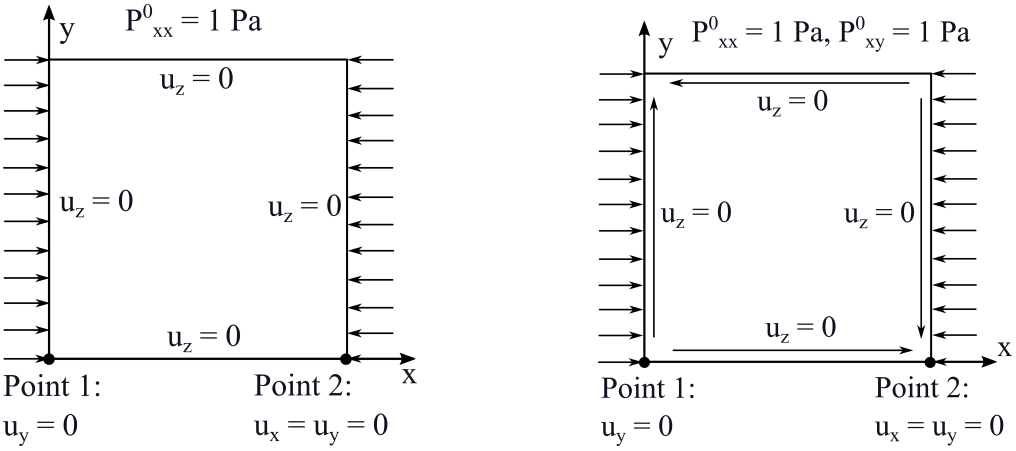

(**a**) Pure compression load. (**b**) Combined compression-shear load.

Figure 10. Boundary and loading conditions, case 2.

Table 5 shows the first four buckling loads for the pure compression case. In this case the model using CLT is able to approximate the results given by Abaqus 3D. Nevertheless, this theory shows a percentage error of 2.7% for the first critical load, which grows up to 4.4% for the fourth critical load. The error on F_1^{cr} can be reduced to 0.04% considering the ED4 model. Through LW models this error can lower than 0.001%. In this case, the best approximation of F_1^{cr} is given by the LM4 model.

Table 5. Critical loads F_i^{cr} [N], pure compression load $P_{xx}^0 = 1$ Pa, case 2.

	$F_1^{cr} \cdot 10^{-3}$	$F_2^{cr} \cdot 10^{-3}$	$F_3^{cr} \cdot 10^{-3}$	$F_4^{cr} \cdot 10^{-3}$
Abaqus 3D	13.63	21.57	35.42	54.46
Ref. [7]	13.63	21.64	35.41	54.56
Ref. [28]	13.67	21.68	35.69	54.60
LM4	13.63	21.57	35.62	54.47
LM2	13.63	21.57	35.62	54.47
LD4	13.63	21.57	35.62	54.47
LD2	13.63	21.57	35.62	54.47
ED4	13.64	21.71	35.80	54.60
ED2	13.67	21.74	35.85	54.81
FSDT	13.84	22.03	36.46	55.47
CLT	14.00	22.35	36.97	56.83

Table 6 shows the first four buckling loads for the compression-shear case. For this loading condition CLT shows an higher maximum error of 7.7% in correspondence of F_4^{cr}. This error is reduced to 1.2% with LD4 and LM4 theories. 0.090% is the minimum error on the first buckling load and is obtained by a LM4 model. It is possible to notice that, because of the combined load case, lower order theories show higher errors in comparison with the pure compression load.

Preprints.org (www.preprints.org) | NOT PEER-REVIEWED | Posted: 16 May 2024 doi:10.20944/preprints202405.1103.v1

Table 6. Critical loads F_i^{cr} [N], compression-shear load $P_{xx}^0 = P_{xy}^0 = 1$ Pa, case 2.

	$F_1^{cr} \cdot 10^{-3}$	$F_2^{cr} \cdot 10^{-3}$	$F_3^{cr} \cdot 10^{-3}$	$F_4^{cr} \cdot 10^{-3}$
Abaqus 3D	12.04	18.46	30.86	41.87
Ref. [7]	12.04	18.49	30.83	41.84
LM4	12.05	18.51	31.03	42.39
LM2	12.05	18.51	31.03	42.39
LD4	12.05	18.51	31.03	42.39
LD2	12.05	18.51	31.03	42.39
ED4	12.07	18.55	31.14	42.56
ED2	12.08	18.58	31.20	42.75
FSDT	12.49	19.31	32.50	44.12
CLT	12.65	19.55	32.98	45.08

3.3. Multilayer Plate with a Central Cut-Out

The third case of analysis is represented by a square multilayer plate with a central circular cut-out. The plate is composed of eight layers, each of them 0.15 mm thick. The in-plane dimensions are $a = b = 254$ mm. The material properties are the same of the second case. The center of the cut-out is placed at $(a/2, b/2)$ and its radius is $r = 40$ mm. Fibers angle distribution is the same of the previous case and the following stack is considered:
$[0 < 60, 15 > |0 < -60, -15 > |0 < -60, -15 > |0 < 60, 15 >]_2$. In this case, the Abaqus reference solution is made of 100′352 elements: 6272 elements are defined into the plane of the plate and 16 elements are defined along the thickness. For CUF results, 72 plate elements have been used. The boundary and loading conditions are the same presented for case 2. Table 7 shows the first four buckling loads for the pure compression load. It is possible to observe that LM theories give the best approximation of F_1^{cr} and F_4^{cr}, while F_2^{cr} and F_3^{cr} are better approximated by LD ones. LM2 shows a minimum error of 0.2% in correspondence of F_1^{cr}, while LM4 shows a minimum error of 0.3% in correspondence of F_4^{cr}. CLT and FSDT models can predict the buckling loads for this case, even though they present higher errors in comparison with other theories.

Table 7. Critical loads F_i^{cr} [N], compression load $P_{xx}^0 = 1$ Pa, case 3.

	$F_1^{cr} \cdot 10^{-2}$	$F_2^{cr} \cdot 10^{-2}$	$F_3^{cr} \cdot 10^{-2}$	$F_4^{cr} \cdot 10^{-2}$
Abaqus 3D	13.322	22.522	31.974	36.974
LM4	13.294	22.386	31.352	37.071
LM2	13.298	22.390	31.360	37.077
LD4	13.378	22.534	31.661	37.280
LD2	13.383	22.539	31.672	37.288
ED4	13.369	22.554	31.763	37.301
ED2	13.420	22.633	31.916	37.432
FSDT	13.562	22.937	32.317	38.092
CLT	13.637	23.144	32.757	38.402

Table 8 shows the first four buckling loads for a compression-shear combined loading. Also in this case the results get progressively closer to the reference solution when LD and LM theories are applied.

Preprints.org (www.preprints.org) | NOT PEER-REVIEWED | Posted: 16 May 2024 doi:10.20944/preprints202405.1103.v1

Table 8. Critical loads F_i^{cr} [N], compression-shear load $P_{xx}^0 = P_{xy}^0 = 1$ Pa, case 3.

	$F_1^{cr} \cdot 10^{-2}$	$F_2^{cr} \cdot 10^{-2}$	$F_3^{cr} \cdot 10^{-2}$	$F_4^{cr} \cdot 10^{-2}$
Abaqus 3D	11.152	19.396	23.956	32.302
LM4	11.146	19.322	23.491	32.337
LM2	11.149	19.326	23.496	32.343
LD4	11.204	19.436	23.638	32.519
LD2	11.207	19.440	23.646	32.526
ED4	11.228	19.490	23.730	32.611
ED2	11.253	19.536	23.808	32.709
FSDT	11.355	19.761	24.078	33.190
CLT	11.416	19.943	24.372	33.519

Even if CLT and FSDT models show a worse approximation of reference solutions, they can correctly match the buckling modes obtained through Abaqus 3D. The buckling modes for the compression-shear case are presented in Figures 11, 12, 13 and 14 where a comparison between Abaqus 3D and LM4 model is shown.

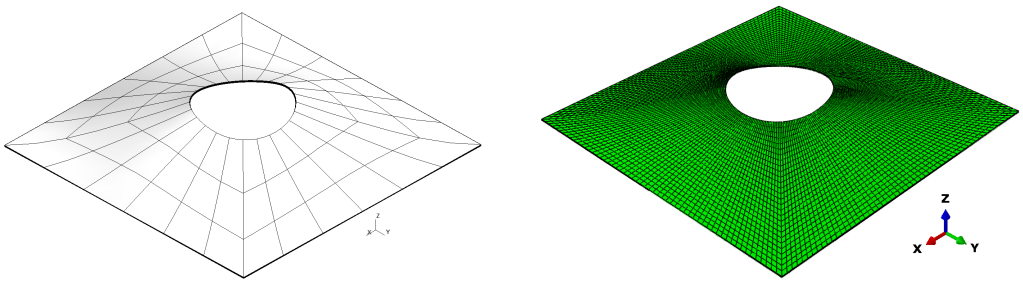

(**a**) LM2 (**b**) Abaqus 3D

Figure 11. First buckling mode, compression-shear load $P_{xx}^0 = P_{xy}^0 = 1$ Pa, case 3.

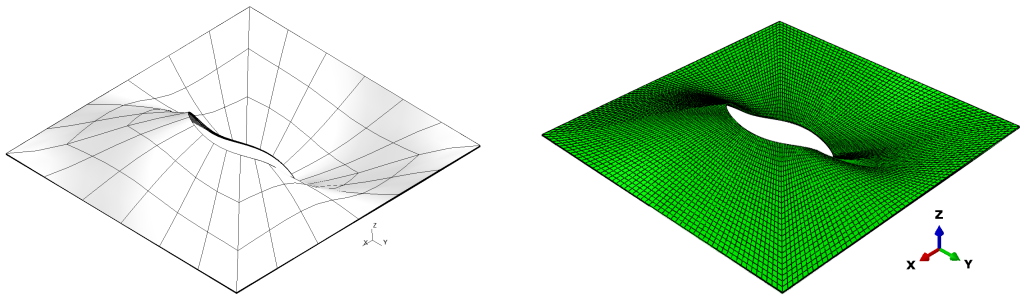

(**a**) LM2 (**b**) Abaqus 3D

Figure 12. Second buckling mode, compression-shear load $P_{xx}^0 = P_{xy}^0 = 1$ Pa, case 3.

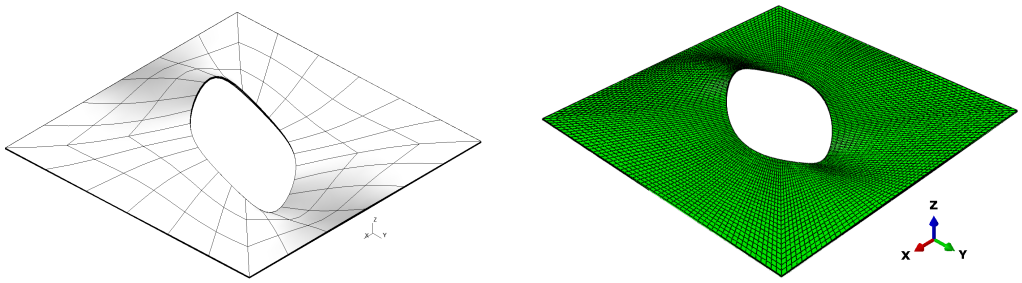

(**a**) LM2 (**b**) Abaqus 3D

Figure 13. Third buckling mode, compression-shear load $P_{xx}^0 = P_{xy}^0 = 1$ Pa, case 3.

Preprints.org (www.preprints.org) | NOT PEER-REVIEWED | Posted: 16 May 2024 doi:10.20944/preprints202405.1103.v1

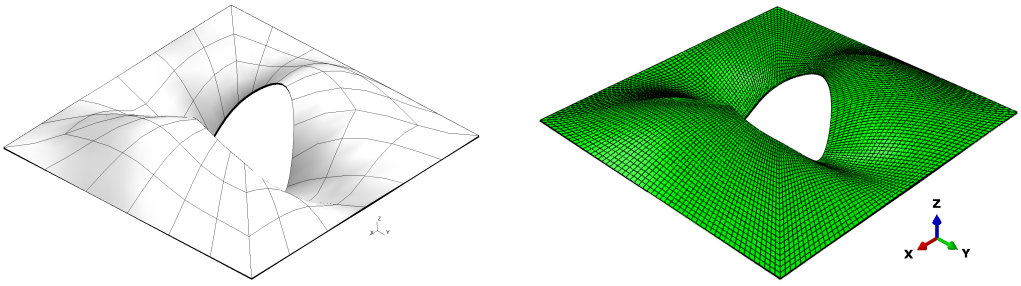

(**a**) LM2 (**b**) Abaqus 3D

Figure 14. Fourth buckling mode, compression-shear load $P^0_{xx} = P^0_{xy} = 1$ Pa, case 3.

4. Conclusions

In this study, linear buckling analyses of VAT plates have been performed by developing two-dimensional CUF finite elements within Reissner's Mixed Variational Theorem. Thanks to its adaptability to a wide range of structural problems and the possibility to choose the approximation theory a-priori, CUF shows a good prediction of buckling loads with an acceptable computational cost. Even though only linear laws have been considered in the numerical simulations for the variation of fibres angle, the implemented numerical framework allows to address a generic variation law. Three numerical examples of plates containing curvilinear fibres have been analyzed and results are compared to Abaqus 3D and literature reference solutions. The comparison among the various results allows to distinguish the developed models according to their accuracy and numerical complexity. Even though CLT and FSDT show a reduced amount of degrees of freadom, allowing to correctly predict buckling loads for the considered benchmark structures 2 and 3, they show a higher loss of accuracy when plates which are not symmetric and balanced are considered, as observed in the first benchmark case. Increasing the through-the-thickness polynomial order, general ESL displacements theories are obtained, which allow to improve the results accuracy. A further improvement in the prediction of buckling loads is obtained through the development of LW displacements models. ESL and LW theories can correctly predict Abaqus 3D results with a limited number of DOF, but being derived from a PVD variational statement show a lack in accuracy for the out-of-plane stresses, which strongly influence the evaluation of the geometric stiffness matrix needed for the linear buckling analysis. Hence, the derivation of LW models to RMVT allows to overcome this problem, enhancing the solution accuracy, specially in the case of the first critical load. Even if LM models allow to improve the prediction of the through-the-thickness behavior, they are characterized by the maximum computational cost among the two-dimensional theories developed in this study, and yet their application is still advantageous mainly when plates characterized by complex stacking sequences are considered especially when compared to the cumberson three-dimensional simulations. In summary, the utilization of RMVT in the context of CUF has demonstrated the potential to enhance the precision and efficiency of modeling VAT plates for buckling analyses. Nevertheless, the scope of this approach extends beyond plate analysis, as there are promising prospects for employing, as a future perspective, this framework in the examination of more challenging VAT structures such as shells.

Author Contributions: Methodology, G.G., D.A.I., L.K. and M.M.; Software, D.A.I.; Validation, D.A.I.; Writing—original draft, D.A.I.; Writing—review & editing, G.G., L.K. and M.M.; Supervision, G.G. and M.M.; Funding acquisition, G.G. and M.M. All authors have read and agreed to the published version of the manuscript.

Funding: This research was funded by the Luxembourg National Research Fund (FNR), grant reference INTER/ANR/21/16215936 GLAMOUR-VSC. For the purpose of open access, and in fulfillment of the obligations arising from the grant agreement, the author has applied a Creative Commons Attribution 4.0 International (CC BY 4.0) license to any Author Accepted Manuscript version arising from this submission. M. Montemurro is grateful to French National Research Agency for supporting this work through the research project GLAMOUR-VSC (Global-LocAl two-level Multi-scale optimisation strategy accOUnting for pRocess-induced singularities to design Variable Stiffness Composites) ANR-21-CE10-0014.

Institutional Review Board Statement: Not applicable.

Informed Consent Statement: Not applicable.

Data Availability Statement: Data will be made available on request.

Preprints.org (www.preprints.org) | NOT PEER-REVIEWED | Posted: 16 May 2024 doi:10.20944/preprints202405.1103.v1

Conflicts of Interest: The authors declare no conflict of interest.

Appendix A. Expression of the Fundamental Nuclei

This appendix reports the FN of the structure stiffness matrix for the PVD and RMVT variational statements. The components of the FN for the PVD case can be written as follows in the case of an orthotropic material:

$$
\begin{aligned}
K_{xx}^{\tau sij} &= \int_\Omega \left(\widetilde{Z}_{pp11}^{\tau s} N_{j,x} N_{i,x} + \widetilde{Z}_{pp16}^{\tau s} N_{j,y} N_{i,x} + \widetilde{Z}_{pp16}^{\tau s} N_{j,x} N_{i,y} + \widetilde{Z}_{pp66}^{\tau s} N_{j,y} N_{i,y} + \widetilde{Z}_{nn44}^{\tau_{rz} s_{rz}} N_j N_i \right) d\Omega \,, \\
K_{xy}^{\tau sij} &= \int_\Omega \left(\widetilde{Z}_{pp12}^{\tau s} N_{j,y} N_{i,x} + \widetilde{Z}_{pp16}^{\tau s} N_{j,x} N_{i,x} + \widetilde{Z}_{pp26}^{\tau s} N_{j,y} N_{i,y} + \widetilde{Z}_{pp66}^{\tau s} N_{j,x} N_{i,y} + \widetilde{Z}_{nn45}^{\tau_{rz} s_{rz}} N_j N_i \right) d\Omega \,, \\
K_{xz}^{\tau sij} &= \int_\Omega \left(\widetilde{Z}_{pn13}^{\tau s_{rz}} N_j N_{i,x} + \widetilde{Z}_{pn36}^{\tau s_{rz}} N_j N_{i,y} + \widetilde{Z}_{nn44}^{\tau_{rz} s} N_{j,x} N_i + \widetilde{Z}_{nn45}^{\tau_{rz} s} N_{j,y} N_i \right) d\Omega \,, \\
K_{yx}^{\tau sij} &= \int_\Omega \left(\widetilde{Z}_{pp12}^{\tau s} N_{j,x} N_{i,y} + \widetilde{Z}_{pp26}^{\tau s} N_{j,y} N_{i,y} + \widetilde{Z}_{pp16}^{\tau s} N_{j,x} N_{i,x} + \widetilde{Z}_{pp66}^{\tau s} N_{j,y} N_{i,x} + \widetilde{Z}_{nn45}^{\tau_{rz} s_{rz}} N_j N_i \right) d\Omega \,, \\
K_{yy}^{\tau sij} &= \int_\Omega \left(\widetilde{Z}_{pp22}^{\tau s} N_{j,y} N_{i,y} + \widetilde{Z}_{pp26}^{\tau s} N_{j,x} N_{i,y} + \widetilde{Z}_{pp26}^{\tau s} N_{j,y} N_{i,x} + \widetilde{Z}_{pp66}^{\tau s} N_{j,x} N_{i,x} + \widetilde{Z}_{nn55}^{\tau_{rz} s_{rz}} N_j N_i \right) d\Omega \,, \\
K_{yz}^{\tau sij} &= \int_\Omega \left(\widetilde{Z}_{pn23}^{\tau s_{rz}} N_j N_{i,y} + \widetilde{Z}_{pn36}^{\tau s_{rz}} N_j N_{i,x} + \widetilde{Z}_{nn45}^{\tau_{rz} s} N_{j,x} N_i + \widetilde{Z}_{nn55}^{\tau_{rz} s} N_{j,y} N_i \right) d\Omega \,, \\
K_{zx}^{\tau sij} &= \int_\Omega \left(\widetilde{Z}_{nn44}^{\tau s_{rz}} N_j N_{i,x} + \widetilde{Z}_{nn45}^{\tau s_{rz}} N_j N_{i,y} + \widetilde{Z}_{np13}^{\tau_{rz} s} N_{j,x} N_i + \widetilde{Z}_{np36}^{\tau_{rz} s} N_{j,y} N_i \right) d\Omega \,, \\
K_{zy}^{\tau sij} &= \int_\Omega \left(\widetilde{Z}_{nn45}^{\tau s_{rz}} N_j N_{i,x} + \widetilde{Z}_{nn55}^{\tau s_{rz}} N_j N_{i,y} + \widetilde{Z}_{np23}^{\tau_{rz} s} N_{j,y} N_i + \widetilde{Z}_{pp36}^{\tau_{rz} s} N_{j,x} N_i \right) d\Omega \,, \\
K_{zz}^{\tau sij} &= \int_\Omega \left(\widetilde{Z}_{nn44}^{\tau s} N_{j,x} N_{i,x} + \widetilde{Z}_{nn45}^{\tau s} N_{j,y} N_{i,x} + \widetilde{Z}_{nn45}^{\tau s} N_{j,x} N_{i,y} + \widetilde{Z}_{nn55}^{\tau s} N_{j,y} N_{i,y} + \widetilde{Z}_{nn33}^{\tau_{rz} s_{rz}} N_j N_i \right) d\Omega \,.
\end{aligned}
\tag{A1}
$$

The subscripts 'x' and 'y' when preceded by a comma refer to the derivative versus the corresponding in-plane direction. The components of the FN for the RMVT case can be written as follows:

$$
\begin{aligned}
K_{uuxx}^{\tau sij} &= \int_\Omega \left(\hat{Z}_{pp11}^{\tau s} N_{j,x} N_{i,x} + \hat{Z}_{pp31}^{\tau s} N_{j,x} N_{i,y} + \hat{Z}_{pp13}^{\tau s} N_{j,y} N_{i,x} + \hat{Z}_{pp33}^{\tau s} N_{j,y} N_{i,y} \right) d\Omega \,, \\
K_{uuxy}^{\tau sij} &= \int_\Omega \left(\hat{Z}_{pp12}^{\tau s} N_{j,y} N_{i,x} + \hat{Z}_{pp32}^{\tau s} N_{j,y} N_{i,y} + \hat{Z}_{pp13}^{\tau s} N_{j,x} N_{i,x} + \hat{Z}_{pp33}^{\tau s} N_{j,x} N_{i,y} \right) d\Omega \,, \\
K_{uuyx}^{\tau sij} &= \int_\Omega \left(\hat{Z}_{pp21}^{\tau s} N_{j,x} N_{i,y} + \hat{Z}_{pp31}^{\tau s} N_{j,x} N_{i,x} + \hat{Z}_{pp23}^{\tau s} N_{j,y} N_{i,y} + \hat{Z}_{pp33}^{\tau s} N_{j,y} N_{i,x} \right) d\Omega \,, \\
K_{uuyy}^{\tau sij} &= \int_\Omega \left(\hat{Z}_{pp22}^{\tau s} N_{j,y} N_{i,y} + \hat{Z}_{pp32}^{\tau s} N_{j,y} N_{i,x} + \hat{Z}_{pp23}^{\tau s} N_{j,x} N_{i,y} + \hat{Z}_{pp33}^{\tau s} N_{j,x} N_{i,x} \right) d\Omega \,, \\
K_{uuxz}^{\tau sij} &= 0 \,, \quad K_{uuyz}^{\tau sij} = 0 \,, \quad K_{uuzx}^{\tau sij} = 0 \,, \quad K_{uuzy}^{\tau sij} = 0 \,, \quad K_{uuzz}^{\tau sij} = 0 \,, \\
K_{u\sigma xx}^{\tau sij} &= \int_\Omega \left(E_{\tau_{rz} s} N_j N_i \right) d\Omega \,, \quad K_{u\sigma xz}^{\tau sij} = \int_\Omega \left(\hat{Z}_{pn13}^{\tau s} N_j N_{i,x} + \hat{Z}_{pn33}^{\tau s} N_j N_{i,y} \right) d\Omega \,, \\
K_{u\sigma yy}^{\tau sij} &= \int_\Omega \left(E_{\tau_{rz} s} N_j N_i \right) d\Omega \,, \quad K_{u\sigma yz}^{\tau sij} = \int_\Omega \left(\hat{Z}_{pn23}^{\tau s} N_j N_{i,y} + \hat{Z}_{pn33}^{\tau s} N_j N_{i,x} \right) d\Omega \,, \\
K_{u\sigma zx}^{\tau sij} &= \int_\Omega \left(E_{\tau s} N_j N_{i,x} \right) d\Omega \,, \quad K_{u\sigma zy}^{\tau sij} = \int_\Omega \left(E_{\tau s} N_j N_{i,y} \right) d\Omega \,, \quad K_{u\sigma zz}^{\tau sij} = \int_\Omega \left(E_{\tau_{rz} s} N_j N_i \right) d\Omega \,, \\
K_{u\sigma xy}^{\tau sij} &= 0 \,, \quad K_{u\sigma yx}^{\tau sij} = 0 \,, \\
K_{\sigma uxx}^{\tau sij} &= \int_\Omega \left(E_{\tau s_{rz}} N_j N_i \right) d\Omega \,, \quad K_{\sigma uxz}^{\tau sij} = \int_\Omega \left(E_{\tau s} N_{j,x} N_i \right) d\Omega \,, \quad K_{\sigma uyy}^{\tau sij} = \int_\Omega \left(E_{\tau s_{rz}} N_j N_i \right) d\Omega \,, \\
K_{\sigma uyz}^{\tau sij} &= \int_\Omega \left(E_{\tau s} N_{j,y} N_i \right) d\Omega \,, \quad K_{\sigma uzx}^{\tau sij} = -\int_\Omega \left(\hat{Z}_{np31}^{\tau s} N_{j,x} N_i - \hat{Z}_{np33}^{\tau s} N_{j,y} N_i \right) d\Omega \,, \\
K_{\sigma uzy}^{\tau sij} &= -\int_\Omega \left(\hat{Z}_{np32}^{\tau s} N_{j,y} N_i - \hat{Z}_{np33}^{\tau s} N_{j,x} N_i \right) d\Omega \,, \quad K_{\sigma uzz}^{\tau sij} = \int_\Omega \left(E_{\tau s_{rz}} N_j N_i \right) d\Omega \,, \\
K_{\sigma uxy}^{\tau sij} &= 0 \,, \quad K_{\sigma uyx}^{\tau sij} = 0 \,, \\
K_{\sigma\sigma xx}^{\tau sij} &= -\int_\Omega \left(\hat{Z}_{nn11}^{\tau s} N_j N_i \right) d\Omega \,, \quad K_{\sigma\sigma xy}^{\tau sij} = -\int_\Omega \left(\hat{Z}_{nn12}^{\tau s} N_j N_i \right) d\Omega \,, \\
K_{\sigma\sigma yx}^{\tau sij} &= -\int_\Omega \left(\hat{Z}_{nn21}^{\tau s} N_j N_i \right) d\Omega \,, \quad K_{\sigma\sigma xx}^{\tau sij} = -\int_\Omega \left(\hat{Z}_{nn22}^{\tau s} N_j N_i \right) d\Omega \,, \\
K_{\sigma\sigma xz}^{\tau sij} &= 0 \,, \quad K_{\sigma\sigma yz}^{\tau sij} = 0 \,, \quad K_{\sigma\sigma zx}^{\tau sij} = 0 \,, \quad K_{\sigma\sigma zy}^{\tau sij} = 0 \,, \quad K_{\sigma\sigma zz}^{\tau sij} = 0 \,.
\end{aligned}
\tag{A2}
$$

Preprints.org (www.preprints.org) | NOT PEER-REVIEWED | Posted: 16 May 2024 doi:10.20944/preprints202405.1103.v1

References

1. H. J. L. Dirk, C. Ward and K. D. Potter. The engineering aspects of automated prepreg layup: History, present and future. *Compos. Part B Eng.* **2012**, *43*, 997–1009.
2. P. Zhuo, S. Li, I. A. Ashcroft and A. I. Jones. Material extrusion additive manufacturing of continuous fiber reinforced polymer matrix composites: A review and outlook. *Compos. Part B Eng.* **2021**, *224*, 109143.
3. M. W. Hyer and H. H. Lee. Innovative design of composite structures: the use of curvilinear fiber format to improve buckling resistance of composite plates with central circular holes. Technical report, 1990.
4. C. J. Brampton, K. C. Wu and H. A. Kim. New optimization method for steered fiber composites using the level set method. *Structural and Multidisciplinary Optimization*, 52:493–505, 2015.
5. Z. Gürdal, B. F. Tatting, and C. K. Wu. Variable stiffness composite panels: effects of stiffness variation on the in-plane and buckling response. *Composites Part A: Applied Science and Manufacturing*, 39(5):911–922, 2008.
6. V. Oliveri and A. Milazzo. A Rayleigh-Ritz approach for postbuckling analysis of variable angle tow composite stiffened panels. *Computers & Structures*, 196:263–276, 2018.
7. P. Hao, X. Yuan, H. Liu, B. Wang, C. Liu, D. Yang and S. Zhan. Isogeometric buckling analysis of composite variable-stiffness panels. *Composite Structures*, 165:192–208, 2017.
8. P. Hao, C. Liu, X. Yuan, B. Wang, G. Li, T. Zhu and F. Niu. Buckling optimization of variable-stiffness composite panels based on flow field function. *Composite Structures*, 181:240–255, 2017.
9. G. Raju, Z. Wu, B. C. Kim and P. M. Weaver. Prebuckling and buckling analysis of variable angle tow plates with general boundary conditions. *Composite Structures*, 94(9):2961–2970, 2012.
10. G. Sciascia, V. Oliveri and P. M. Weaver. Eigenfrequencies of prestressed variable stiffness composite shells. *Composite Structures*, 270:114019, 2021.
11. X. Chen, Z. Wu, G. Nie and P. Weaver. Buckling analysis of variable angle tow composite plates with a through-the-width or an embedded rectangular delamination. *International Journal of Solids and Structures*, 138:166–180, 2018.
12. Z. Wu, G. Raju and P. M. Weaver. Framework for the buckling optimization of variable-angle tow composite plates. *AIAA Journal*, 53(12):3788–3804, 2015.
13. M. Montemurro. An extension of the polar method to the first-order shear deformation theory of laminates. *Composite Structures*, 127:328–339, 2015.
14. M. Montemurro. The polar analysis of the third-order shear deformation theory of laminates. *Composite Structures*, 131:775–789, 2015.
15. M. Montemurro and A. Catapano. On the effective integration of manufacturability constraints within the multi-scale methodology for designing variable angle-tow laminates. *composite structures*, 161:145–159, 2017.
16. A. Catapano, M. Montemurro, J.-A. Balcou, and E. Panettieri. Rapid prototyping of variable angle-tow composites. *Aerotecnica Missili & Spazio*, 98(4):257–271, 2019.
17. M. Montemurro and A. Catapano. A general b-spline surfaces theoretical framework for optimisation of variable angle-tow laminates. *Composite Structures*, 209:561–578, 2019.
18. G. A. Fiordilino, M. I. Izzi, and M. Montemurro. A general isogeometric polar approach for the optimisation of variable stiffness composites: Application to eigenvalue buckling problems. *Mechanics of Materials*, 153:103574, 2021.
19. E. Carrera. Theories and finite elements for multilayered, anisotropic, composite plates and shells. *Archives of Computational Methods in Engineering*, 9(2):87–140, 2002.
20. E. Carrera. Theories and finite elements for multilayered plates and shells: a unified compact formulation with numerical assessment and benchmarking. *Archives of Computational Methods in Engineering*, 10(3):215–296, 2003.
21. E. Carrera, G. Giunta, and S. Brischetto. Hierarchical closed form solutions for plates bent by localized transverse loadings. *Journal of Zhejiang University-SCIENCE A*, 8:1026–1037, 2007.
22. E. Carrera and G. Giunta. Hierarchical models for failure analysis of plates bent by distributed and localized transverse loadings. *Journal of Zhejiang University-SCIENCE A*, 9:600–613, 2008.
23. G. Giunta, A. Catapano, and S. Belouettar. Failure indentation analysis of composite sandwich plates via hierarchical models. *Journal of Sandwich Structures & Materials*, 15(1):45–70, 2013.

Preprints.org (www.preprints.org) | NOT PEER-REVIEWED | Posted: 16 May 2024 doi:10.20944/preprints202405.1103.v1

24. G. Gaetano, B. Salim, B. Fabio, C. Erasmo. Hierarchical theories for a linearised stability analysis of thin-walled beams with open and closed cross-section. *Advances in aircraft and spacecraft science*, 1(3):253, 2014.
25. Y. Hui, R. Xu, G. Giunta, G. De Pietro, H. Hu, S. Belouettar and E. Carrera. Multiscale CUF-FE2 nonlinear analysis of composite beam structures. *Computers & Structures*, 221:28–43, 2019.
26. Y. Hui, X. Bai, Y. Yang, J. Yang, Q. Huang, X. Liu, W. Huang, G. Giunta and H. Hu. A data-driven CUF-based beam model based on the tree-search algorithm. *Composite Structures*, 300:116123, 2022.
27. A. Viglietti, E. Zappino, and E. Carrera. Analysis of variable angle tow composites structures using variable kinematic models. *Composites Part B: Engineering*, 171:272–283, 2019.
28. N. Fallahi, A. Viglietti, E. Carrera, A. Pagani, and E. Zappino. Effect of fiber orientation path on the buckling, free vibration, and static analyses of variable angle tow panels. *Facta Universitatis. Series: Mechanical Engineering*, 18(2):165–188, 2020.
29. N. Fallahi, E. Carrera, and A. Pagani. Application of ga optimization in analysis of variable stiffness composites. *International Journal of Materials and Metallurgical Engineering*, 15(2):65–70, 2021.
30. A. R. Sanchez-Majano, A. Pagani, M. Petrolo, and C. Zhang. Buckling sensitivity of tow-steered plates subjected to multiscale defects by high-order finite elements and polynomial chaos expansion. *Materials*, 14(11):2706, 2021.
31. A. Pagani and A. R. Sanchez-Majano. Influence of fiber misalignments on buckling performance of variable stiffness composites using layerwise models and random fields. *Mechanics of Advanced Materials and Structures*, 29(3):384–399, 2022.
32. L. Demasi, Y. Ashenafi, R. Cavallaro, and E. Santarpia. Generalized unified formulation shell element for functionally graded variable-stiffness composite laminates and aeroelastic applications. *Composite Structures*, 131:501–515, 2015.
33. R. Vescovini and L. Dozio. A variable-kinematic model for variable stiffness plates: Vibration and buckling analysis. *Composite Structures*, 142:15–26, 2016.
34. E. Carrera and L. Demasi. Classical and advanced multilayered plate elements based upon pvd and rmvt. part 1: Derivation of finite element matrices. *International Journal for Numerical Methods in Engineering*, 55(2):191–231, 2002.
35. E. Carrera and L. Demasi. Classical and advanced multilayered plate elements based upon pvd and rmvt. part 2: Numerical implementations. *International Journal for Numerical Methods in Engineering*, 55(3):253–291, 2002.
36. G. Giunta, D. A. Iannotta and M. Montemurro. A FEM Free Vibration Analysis of Variable Stiffness Composite Plates through Hierarchical Modeling. *Materials*, 16(13):4643, 2023.
37. D. A. Iannotta, G. Giunta and M. Montemurro. A mechanical analysis of variable angle-tow composite plates through variable kinematics models based on Carrera's unified formulation. *Composite Structures*, 327:117717, 2024.
38. J. N. Reddy. *Mechanics of laminated composite plates and shells: theory and analysis*. CRC press, 2003.
39. E. Carrera. On the use of the murakami's zig-zag function in the modeling of layered plates and shells. *Computers & Structures*, 82(7-8):541–554, 2004.
40. K.-J. Bathe. *Finite element procedures*. Klaus-Jurgen Bathe, 2006.

Disclaimer/Publisher's Note: The statements, opinions and data contained in all publications are solely those of the individual author(s) and contributor(s) and not of MDPI and/or the editor(s). MDPI and/or the editor(s) disclaim responsibility for any injury to people or property resulting from any ideas, methods, instructions or products referred to in the content.